GEOPHYSICS®

Application of high-order FEM to the P-wave propagation around and inside an underground cavity

Journal:	*Geophysics*
Manuscript ID	GEO-2016-0447.R2
Manuscript Type:	Technical Paper
Date Submitted by the Author:	03-Apr-2017
Complete List of Authors:	Esterhazy, Sofi; Universitat Wien Fakultat fur Mathematik, ; Universitat Wien Fakultat fur Geowissenschaften Geographie und Astronomie, Departement of Meteorology and Geophysics Schneider, Felix; Universitat Wien Fakultat fur Geowissenschaften Geographie und Astronomie, Department of Meteorology and Geophysics Perugia, Ilaria; Universitat Wien Fakultat fur Mathematik Bokelmann, Götz; University of Vienna, Department of Meteorology and Geophysics
Keywords:	compressional wave (P-wave), finite element, frequency-domain, wave equation, two-dimensional
Area of Expertise:	Seismic Modeling and Wave Propagation, Geophysical Software and Algorithms
Note: The following files were submitted by the author for peer review, but cannot be converted to PDF. You must view these files (e.g. movies) online.	
Table1.tex	

Application of high-order FEM to the P-wave propagation around and inside an underground cavity

Sofi Esterhazy[1,2], Felix Schneider[2], Ilaria Perugia[1], Götz Bokelmann[2]

[1] *University of Vienna, Faculty of Mathematics, Vienna, Austria.*

E-mail: sofi.esterhazy@univie.ac.at, ilaria.perugia@univie.ac.at

[2] *University of Vienna, Faculty of Earth Sciences, Geography and Astronomy, Department of Meteorology and Geophysics, Vienna, Austria*

E-mail: felix.schneider@univie.ac.at, goetz.bokelmann@univie.ac.at

(April 20, 2017)

GEO-2016-0447

Running head: **Wave propagation around a cavity**

ABSTRACT

In this paper we study the scattering of P-waves from an acoustic inclusion in a 2D half-space with free surface. The motivation for this study comes from detecting a cavity which might be caused by a underground nuclear explosion (UNE). This is relevant to the On-Site Inspection (OSI), an element of the Comprehensive Nuclear-Test Ban Treaty (CTBT). The waveform modeling we address is implemented in the frequency domain, i.e. we consider the wavefield as well as the source to be time-harmonic. We numerically investigate the cases where the source of the scattered

field is either a plane wavefrom the bottom or the side as from a passive sources like teleseismic waves or ambient noise or a spherical wavefrom the surface as from an active point sources like a vibroseis or an explosion. To this end we split the total field in an incident and an unknown scattered field in order to understand the effects more explicitly. Modeling the response of a void in a medium is not trivial and many numerical algorithms commonly used for seismic propagation modeling will fail. We want to highlight therefore the advantage of high-order methods for this type of applications in general and demonstrate the benefit by using the FEM code Ngsolve. This is in particular the case for the situation we have at hand where the ratio between the size and the depth of the cavity is notably high. In our study we address this scenario numerically in the first place, as there are few field observations of the effects and the number of papers addressing the theoretical basis is sparse. Finally, we find that our splitting strategy together with the numerical scheme that we apply give rise to a constructive approach for studying this specific issue.

INTRODUCTION

The numerical simulation of wavefield propagation has many applications in geophysics, in particular for the study of the complex behavior of seismic waves through some heterogeneous underground structures such as gas or oil reservoirs, sinkholes (Tran et al., 2013), clandestine tunnels (Sloan et al., 2015), old mine workings (Gritto, 2003) or cavities caused by a nuclear explosion (Richards and Zavales, 1990). The latter is of interest to us due to the need to detect nuclear explosions set offwithin the Earth, i.e. underground. This need arises from the future Comprehensive Nuclear Test-Ban Treaty (CTBT). In order to put the Treaty in force, treaty violations need to be verifiable. An important ingredient of this is the On-site Inspection (OSI) part of the CTBT, where a group of up to 40 scientific experts investigate a designated suspicious area for a limited amount of time, searching for evidence of an underground nuclear explosion (UNE), and thus testing the compliance with the treaty in the field. The underlying technical questions of the OSI are still quite new and a strong scientific groundwork is pending. So far, there are only few experimental examples that have been suitably documented to build a proper scientific groundwork. The techniques comprise the entire spectrum of applied geophysics; a key is to detect the anomalous structures in the subsurface using various kinds of man-made or naturally-created seismic waves. We thus study the interaction of seismic waves with underground cavities, using a simple model of a spherical cavity.

Some theoretical approaches have been discussed for the scattering problem of a fluid-filled cavity (Korneev, 2009) in an elastic medium, but very few discussions on the theory have been provided in a field context (Rechtien et al., 1976), in particular for the special case of nuclear verification. Some reasons for this lack might be the excessive costs as well as the absence of suitable cavities where the conditions and precise location are already known for a scientific verification. Furthermore, testing these techniques comes at an extremely expensive cost. This motivates the investigation of the problem on a purely numerical level and the simulation of potential observations based on recent advances in numerical modeling of wave propagation problems.

For the numerical computations we want to motivate the use of high-order finite element methods (in contrast to low order methods with a comparable number of degrees of freedom). Prevalent methods for local problems used in geophysics are the spectral element method (Faccioli et al., 1997; Komatitsch and Vilotte, 1998; Komatitsch and Tromp, 2002) and also the spectral discontinous Galerkin method (Antonietti et al., 2014) as part of the family of high-order methods in geophysics. Alternative options include methods based on boundary layer theory (e.g. Mei et al., 1984), multipole expansions (e.g. Imhof, 2004) and boundary integral formulations (e.g. Pointer et al., 1998).

We approximate a complex subsurface structure by a simplified geometry of a homogeneous half-space with a spherical inclusion (Figure 1). As we seek to investigate the wave propagation on a local scale, one needs the domain of interest and some suitable conditions on the artificial boundary. Here, the perfectly matched layer (PML) method is a suitable solution for both, plane waves as well as spherical waves in the presence of a free surface. With the cavity being small compared to the surrounding media, the interface is very curved. This geometric feature suggests to use triangles for a regular/good discretization. Our computations are done with the parallel High-Order Finite Element Library Ngsolve ontop of the automatic 2D/3D tetrahedral mesh generator Netgen (Schöberl, 1997, 2014).

Accurate numerical modeling can help to create observational strategies for detecting the presence of an underground (nuclear) cavity and improve the protocols for OSI field deployments. Appropriately addressing the phenomena of wave propagation around an underground cavity in a mathematical sense will thus help to set a proper scientific base of OSI and contribute to bringing the Treaty into force.

In this paper we first specify the mathematical formulation of our model problem introducing the governing equations, a suitable treatment on the boundary of the computational domain, and a description of the sources that are taken into account. Then we give a detailed formulation of our numerical approach and discuss the stability for our numerical model. Finally we present numerical examples for some specific cases of a point source in the near-field and a plane wave coming from the far-field.

PROBLEM FORMULATION

Geometry design

The model we use for our computations is described in in Table 1 and Figure 1. It is based on the representation of a cavity caused by a possible underground nuclear explosion (UNE). In general, these are not spherical. In most cases, the void created by the initial explosion will collapse and create an elongated vertical chimney filled with rubble. If the chimney does not extend to the surface, as would be the case for an event that necessitates an OSI, the upper point of the chimney will have a void (apical void) at the top. Of course, sometimes a cavity is created (e.g. the GNOME explosion, Rawson et al., 1964). To detect the cavity as a remnant of an UNE would be a significant contribution to an OSI.

This simplistic model, however, gives already valuable information in term of numerical requirements and carries the essential features of the problem at hand. The challenge is to model the behavior of the wave interaction correctly over a broad range of frequencies, e.g. from the static regime to scattering at high frequencies, including eigenoscillations. This allows us to propose the best strategy for detecting deeply buried cavities.

Governing equations

We consider the 2D time-harmonic acoustic wave propagation problem

$$\nabla \cdot \left(\frac{1}{\rho(\mathbf{x})} \nabla p(\mathbf{x}) \right) + \frac{\omega^2}{\rho(\mathbf{x}) v(\mathbf{x})^2} p(\mathbf{x}) = 0 \quad \text{in } \tilde{\Omega} \tag{1}$$

for the scalar-valued pressure field p with an angular frequency $\omega > 0$ in the unbounded half plane $\tilde{\Omega} = \{\mathbf{x} := (x, y) \in \mathbb{R}^2 : \; y < 0\}$ which is partitioned into two subdomains,Ω_1 and $\tilde{\Omega}_2$ as depicted in Figure 1. The domain-wise constant functions

$$v(\mathbf{x}) = \begin{cases} v_1 & \text{in}\Omega_1 \\ v_2 & \text{in } \tilde{\Omega}_2 \end{cases}, \; \rho(\mathbf{x}) = \begin{cases} \rho_1 & \text{in}\Omega_1 \\ \rho_2 & \text{in } \tilde{\Omega}_2 \end{cases} \tag{2}$$

represent the characteristic speed of sound and the density, respectively, of the medium. An example of choice of material and geometry parameters, which will be used in the numerical tests reported in the following is given in Table 1. For the following, we also define the domain-wise constant wavenumber by

$$k(\mathbf{x}) = \begin{cases} k_1 = \omega/v_1 & \text{in}\Omega_1 \\ k_2 = \omega/v_2 & \text{in } \tilde{\Omega}_2 \end{cases}. \tag{3}$$

Let us now assume that a known incident wavefield p_{inc} satisfies the Helmholtz equation (1) in the homogeneous full space with $v \equiv v_2$ (and ρ arbitrary, but constant) and split the total wavefield into the incident and a scattered wavefield as $p = p_{inc} + p_{scat}$. Then the equation for the remaining unknown p_{scat} in the outer domainΩ_2 looks like:

$$\nabla \cdot \left(\frac{1}{\rho_2}\nabla p_{scat}\right) + \frac{k_2^2}{\rho_2} p_{scat} = -\nabla\cdot \left(\frac{1}{\rho_2}\nabla p_{inc}\right) - \frac{k_2^2}{\rho_2} p_{inc} = 0 \quad \text{in } \Omega_2, \tag{4}$$

while we obtain an inhomogeneous contribution of the right hand side for the domain Ω_1:

$$
\begin{aligned}
\nabla \cdot \left(\frac{1}{\rho_1}\nabla p_{scat}\right) + \frac{k_1^2}{\rho_1} p_{scat} &= -\nabla \cdot \ \left(\frac{1}{\rho_1}\nabla p_{inc}\right) - \frac{k_1^2}{\rho_1} p_{inc} + \frac{k_2^2}{\rho_1} p_{inc} - \frac{k_2^2}{\rho_1} p_{inc} \\
&= \underbrace{-\nabla \cdot \ \left(\frac{1}{\rho_1}\nabla p_{inc}\right) - \frac{k_2^2}{\rho_1} p_{inc}}_{=0} - \frac{k_1^2}{\rho_1} p_{inc} + \frac{k_2^2}{\rho_1} p_{inc} \\
&= \qquad - \left(\frac{k_1^2}{\rho_1} - \frac{k_2^2}{\rho_1}\right) p_{inc} \quad \text{in} \Omega_{\ 1},
\end{aligned} \tag{5}
$$

Thus, the remaining unknown p_{scat} solves the following in-homogeneous problem

$$
\nabla \cdot \left(\frac{1}{\rho(\mathbf{x})}\nabla p_{scat}\right) + \frac{k^2(\mathbf{x})}{\rho(\mathbf{x})} p_{scat} = \Psi_{scat} \quad \text{in } \tilde{\Omega}, \tag{6}
$$

where the right hand side is defined domain-wise as

$$
\Psi_{scat}(\mathbf{x}) = \begin{cases} -\frac{1}{\rho_1}(k_1^2 - k_2^2) p_{inc} & \text{in} \Omega_{\ 1} \\ 0 & \text{in } \tilde{\Omega}_2 \end{cases} . \tag{7}
$$

Boundary and far-field conditions

We assume the homogeneous Dirichlet boundary condition $p = 0$ on the surface $\Gamma := \{\mathbf{x} = (x, y) \in \mathbb{R}^2 : \ y = 0\}$, which translates into the inhomogeneous boundary condition

$$
p_{scat} = -p_{inc}. \tag{8}
$$

The half-space problem is completed by the outgoing Sommerfeld radiation condition. For the numerical computation, however, we truncate the unbounded domain $\tilde{\Omega}_2$ to a finite domain Ω_2 as shown in Figure 2 and impose some artificial condition on the emerging boundary. Here, we use the Perfectly Matched Layer (PML) method (Berenger, 1994) which adds a layer around the artificial boundary where a complex coordinate transformation is applied so that all outgoing waves get absorbed. To the simplest degree, denoting by ν the coordinate normal to the interface between Ω_2 and Ω_{PML} with positive direction pointing inside Ω_{PML}, and taking $\nu = 0$ at the interface, this coordinate transformation can be expressed as

$$\tilde{\nu} = \Phi_{\mathrm{PML}}(\nu) = \nu + i \int_0^{\nu} \sigma(t)dt, \tag{9}$$

where $\sigma(t)$ is a function such that $\sigma(t) = 0$ outside Ω_{PML} and $\sigma(t) > 0$ in Ω_{PML}. The coordinate tangential to the interface remains unchanged. In our case we simply chose $\sigma(t) = \sigma_0$ (constant) in Ω_{PML}. For details on the PML technique in Cartesian geometries, we refer to Bramble and Pasciak (2013). There, the Cartesian PML was proven to be stable provided that the product $L\sigma_0$ is sufficiently large where L is the width of the boundary layer.

Source excitation

We consider the source to be a point source either located on Γ in the vicinity of Ω_1 or somewhere at infinity in $\tilde{\Omega}_2$. In both cases, we are assuming the source to be harmonic in time. Therefore, we only define the space-dependent factor of the incident field. In the first case, denoting by $(x_0, y_0) \in \Gamma$ the location of the point source and setting $\tilde{r} = \sqrt{(x - x_0)^2 + (y - y_0)^2}$, the incident field is a spherical wave given by

$$p_{inc}(\mathbf{x}) = \frac{a k_2^2 i}{4} H_0^{(1)}(k_2 \tilde{r}), \tag{10}$$

where $H_0^{(1)}$ is the Hankel function of first kind, zeroth order and $a \in \mathbb{R}^+$ an amplification factor (McLean, 2000, p. 282). Note also that here p_{inc} is the Green's function of the 2D acoustic wave/Helmholtz equation with wavenumber k_2. In the second case, the incident field is a plane wave given by

$$p_{inc}(\mathbf{x}) = ak_2 e^{i(\cos(\alpha)k_2 x + \sin(\alpha)k_2 y)} \tag{11}$$

with α is the angle of incidence, and again $a \in \mathbb{R}^+$.

FINITE ELEMENT APPROXIMATION

For the numerical computation we chose to use the Finite Element Method (FEM) which is a powerful computational method with high flexibility regarding the underlying geometry. In particular, we will use high-order elements which, in the case of the time-harmonic wave problems with high wavenumbers, deliver a higher accuracy, as compared to low order schemes with the same number of degrees of freedom (Esterhazy and Melenk, 2012). We point out that in the context of acoustic equations in the time domain a similar situation occurs; see e.g. (Seriani and Priolo, 1994; Cohen, 2002; Ainsworth, 2004; De Basabe and Sen, 2007). We used the software package NGSOLVE, an open source, parallel, high-order finite element library on top of the mesh handler NETGEN developed by Joachim Schöberl (Schöberl, 2014, 1997). NGSOLVE is written in C++11 and contains a rich Python interface to control the program flow as well as the geometry description and the equation setup.

The variational formulation

The finite element method is based on a variational formulation of the problem. In order to derive it for problem (6), we multiply the equations by a test function and integrate over the computational domain $\Omega := \Omega_1 \cup \Omega_2 \cup \Omega_{\mathrm{PML}}$ and denote by J_{PML} the Jacobian of the PML coordinate transformation Φ_{PML} and by D_{PML} the determinant of J_{PML} ($J_{\mathrm{PML}}^{-\top}$ denotes the transpose of the inverse of J_{PML}). Then the weak formulation reads:

$$\begin{aligned} &\text{Find } p_{scat} \in H^1(\Omega) \text{ s.t. } p_{scat} = -p_{inc} \text{ on} \Gamma \text{and} \\ &B(p_{scat}, v) = l(v) \quad \forall v \in H^1_\Gamma(\Omega) \end{aligned} \tag{12}$$

where

$$\begin{aligned} B(p_{scat}, v) = &\int_{\Omega_1} \left(\frac{1}{\rho_1} \nabla p_{scat} \cdot \nabla v + \frac{k_1^2}{\rho_1} p_{scat} v \right) \, d\mathbf{x} \\ &+ \int_{\Omega_2} \left(\frac{1}{\rho_2} \nabla p_{scat} \cdot \nabla v + \frac{k_2^2}{\rho_2} p_{scat} v \right) \, d\mathbf{x} \\ &+ \int_{\Omega_{\mathrm{PML}}} \frac{1}{\rho_2} (J_{\mathrm{PML}}^{-\top} \nabla p_{scat}) \cdot (J_{\mathrm{PML}}^{-\top} \nabla v) D_{\mathrm{PML}} \, d\mathbf{x} \\ &+ \int_{\Omega_{\mathrm{PML}}} \frac{k_2^2}{\rho_2} p_{scat} v D_{\mathrm{PML}} \, d\mathbf{x} \end{aligned}$$

and

$$l(v) = \int_\Omega \Psi_{scat} v \, d\mathbf{x} = -\frac{k_2^2 - k_1^2}{\rho_1} \int_{\Omega_1} p_{inc} v \, d\mathbf{x} \tag{13}$$

The function spaces are defined by

$$H^1(\Omega) := \{ p \in L^2(\Omega) \mid \nabla p \in L^2(\Omega) \} \tag{14}$$

and

$$H^1_\Gamma(\Omega) := \{ p \in H^1(\Omega) \mid p = 0 \text{ on } \Gamma \}. \tag{15}$$

Depending on the choice of source the method is also slightly adapted as discussed in the following section.

The discrete formulation

For the finite element discretization, we partition the computational domain Ω with a mesh containing a finite number of elements:

$$\mathcal{T}_h := \{K \mid \operatorname{diam}(K) < h, \bigcup K = \bar{\Omega}\}. \tag{16}$$

We introduce the space of continuous functions

$$\mathbb{P}_\ell(\mathcal{T}_h) = \{v \in C^0(\Omega) : v|_K \in \mathbb{P}_\ell(K)\ \forall K \in \mathcal{T}_h\} \tag{17}$$

where $\mathbb{P}_\ell(K)$ is the space of polynomials of degree at most ℓ on K. Then, the discrete formulation reads

$$\begin{gathered}\text{Find } p^N_{scat} \in \mathbb{P}_\ell(\mathcal{T}_h) \text{ s.t. } p^N_{scat} = -p^N_{inc} \text{ on} \Gamma \text{and} \\ B(p^N_{scat}, v^N) = l(v^N) \quad \forall v^N \in V_N\end{gathered} \tag{18}$$

with $p^N_{inc} \in \mathbb{P}_\ell(\mathcal{T}_h)$ being the interpolation of p_{inc} in $\mathbb{P}_\ell(\mathcal{T}_h)$ and $V_N := \mathbb{P}_\ell(\mathcal{T}_h) \cap H^1_0(\Omega)$ with $N = N(h,\ell)$ being the total number of degrees of freedom. With $\{\varphi_j\}_{j=1}^N$ being a basis of V_N and using the ansatz $p_{scat} = \sum_{j=1}^N p_j \varphi_j, v = \sum_{j=1}^N v_j \varphi_j$, (18) reduces to a linear system

$$\mathbf{B}\mathbf{p} = \mathbf{l} \tag{19}$$

where $\mathbf{B} = [B(\varphi_j, \varphi_i)]_{i,j=1}^N$ and $\mathbf{l} := [l(\varphi_i)]_{i=1}^N$ can be computed explicitly and $\mathbf{p} = [p_i]_{i=1}^N$ is the unknown coefficient vector to be computed. In Ngsolve we use the

C^0 continuous expansion of Legendre–Dubiner basis (Dubiner, 1991; Sherwin and Karniadakis, 1995) with Gauss-Legendre quadrature.

Numerical issues

The numerical approximation of the time-harmonic wave problem is challenging when the product of wavenumber and domain size is large. In fact, the solutions display oscillations with wavelength proportional to the inverse of the wavenumber. It is well-known that the classic FEM (but the situation would not be different with the finite difference method) suffer of the so-called *pollution effect* (Babuška and Sauter, 1997): Keeping the ratio between the mesh size and the wavelength constant, piecewise linear elements guarantee good approximation properties of the FEM space, yet it does not guarantee convergence of the FEM approximation. In the context of computational seismology this means that the same spatial discretization is less accurate for higher incident frequencies. However, it can be shown that a stronger condition, namely a mesh size proportional to the square of the wavelength (Bayliss et al., 1985; Ihlenburg and Babuška, 1995) leads to quasi-optimality, i.e. the solution up to a constant that is independently of the wavenumber as good as the best approximation.

The situation is mitigated in the case of higher order FEM, where similar accuracy can be obtained with less degrees of freedom. The better convergence for higher order FEM is shown in Figure 3 as well as in Figure 4, where it is also clear that the pre-asymptotic region (before convergence takes place) is wider for lower degrees. We first demonstrate the convergence of the FEM solution by testing against a refined FEM solution on a finer mesh and with higher polynomial degree. In addition, we verify the convergence for a case of a cylindrical vacuum cavity in the surface-free space where an analytic solution is known by (Colton and Kress, 1983; Bin-Mohsin, 2013, p. 39)

$$u(r,\theta) = J_0 - \frac{J_0(ka)H_0^{(1)}(kr)}{H_0^{(1)}(ka)} + \sum_{n=1}^{\infty} i^n \cos(n\theta)\left[J_n(kr) - \frac{J_n(ka)H_n^{(1)}(kr)}{H_n^{(1)}(ka)}\right], \quad (20)$$

for $(r,\theta) \in \mathbb{R}^2 \backslash B(0;a)$, i.e. $r \geq a, \theta \in [0, 2\pi)$ and $J_n, H_n^{(1)}$ are the Bessel and Hankel function of first kind of order n, respectively.

The improvement is remarkable when comparing e.g. approximations obtained with linear and cubic polynomials. In this computation the advantage of using polynomials of degree 1 versus 2, or 3 versus 4 seems less visible. This behavior can be traced back to the fact that the width of the PML region was chosen to be the same for all polynomial degrees. A wavenumber-explicit convergence analysis (Melenk and Sauter, 2010, 2011; Esterhazy and Melenk, 2012, 2014) shows that for the classical hp-FEM one can obtain the quasi-optimality under the condition that hk/p is sufficiently small and p is at least $\mathcal{O}(\log k)$ (if the solution operator of the Helmoltz problem is bounded by a constant which polynomially depends on k).

We therefore chose the FEM parameters as well as the PML parameters in dependence of the frequency $f = \omega/2\pi$. In particular and in accordance to the findings mentioned above we chose the polynomial degree $p = \max\{2, \lceil\log(k)\rceil\}$ and the mesh size $h = cp/k$ with $c := \pi/4$. Notice that, due to equation (3), the same h and p are used inΩ_2 andΩ_{PML}. The mesh size inside the cavity is fine according to the slower material velocity. We carried out the time-harmonic computations for a wide range of frequencies in order to reproduce the time-dependent problem. Our numerical calculations were conducted on the VSC3, one of the multi-core machines of the Vienna Scientific Cluster. There, we occupied 16 nodes and split the full range of frequencies into 16 equal sub-intervals of frequencies, spreading one subsection to each node. For computational simplification we then built only one mesh on each node such that the grid size suit to the smallest frequency in the sub-interval while the PML width L was chosen sufficiently for the lowest wavenumber in the according sub-interval.

We have chosen the function σ in the PML transformation in equation (9) as $\sigma(t) \equiv 1$. As the amplitude of the wavefield increases with respect to the frequency, we cannot expect to scale the PML width linearly to the wavelength in order to obtain the same level of absorption at the outer edge of the computational domain. In particular for our purpose we found it to be suitable to choose the following correlation for the PML width $L = v_2/\sqrt{2\pi f} = v_2/\sqrt{\omega} = \sqrt{2\pi v_2 \lambda}$. We show in Figure 5 that, for different values of frequency f, the PML selected according to this rule induces more or less the same level of absorption of the wavefield.

SEISMIC WAVE COMPUTATIONS

To present our findings, we illustrate our method according to the parameters given in Table 1 and the model problem defined in equation (6). In Figure 6 are shown the geometry and the according mesh generated by NGSOLVE.

As mentioned in the introduction, our motivation for considering the above described model problem comes from seismic applications. For this reason, we will be interested in the displacement field

$$\mathbf{u}(\mathbf{x},\omega) = \frac{1}{\rho(\mathbf{x})\omega^2}\nabla p(\mathbf{x}). \tag{21}$$

In addition to that, seismograms at a particular position $\hat{\mathbf{x}}$ at the surface are build by inverse Fourier transform. We are able to sample the incoming frequency over a large and dense range. This gives us an insight into the interplay of the wavefield within and outside of the cavity. In particular, for our model we sampled the incoming frequency from 0.1 to 64 Hz with a rate of 1/10 Hz. In our experiments, we have chosen the material parameters according to Table 1. The parameters for Ω_1 represent the properties of a water-filled cavity, while the parameters for Ω_2 can be associated to a material such as sandstone ore limestone (Bourbié and Coussy, 1987).

Note that the problem is solved in the pressure formulation. However, the visualization of the wavefield at the surface is not possible for the pressure field due to the presence of the free surface. Hence, we derive the displacement field from the pressure field using the expression in equation (21). From the displacement field we construct the seismograms set up by harmonic composition of the displacement field spectra at any particular point of interest due to the continuous solution at hand. We show only the vertical components of the displacement at the free surface, since for the acoustic case there is no contribution in the horizontal component. The seismograms of the incoming, scattered, and total field are given along the surface from -2000 m to 2000 m distance from the cavity center with a spacing of 50 m far from and 30 m in the vicinity of the cavity. The spacing above the cavity is a little denser in order to better resolve the area near the vertex of the refracted wave.

In the following, we describe the application for the two types of sources which were mentioned in previous section.

Example for a passive seismic source

In this example we illustrate the case of a plane wave coming from the bottom left with an angle $\alpha = 3\pi/8 = 67.5$ degree from the horizontal, see equation (11).

Note that in this case we split offthe incident wave and the surface reflection from the total wavefield such that $p_{tot} = p_{inc} + p_{surf} + p_{scat}$, in order to avoid a numerical artificial shadow zone due to the absorbing layer. In particular, the plane wave reflected at the surface is then given by

$$p_{surf} = -ae^{i(\cos(\alpha)k_2 x - \sin(\alpha)k_2 y)}. \tag{22}$$

Consequently, the remaining unknown p_{scat} takes only into account the scattering originated solely by the cavity.

In Figure 7 is shown the horizontal and the vertical component of the incident wavefield; measured as plane waves in the surface. The incoming wavefield is given as a plane wave in the full space, measured along a line equivalent to the surface and therefore has a contribution the both components, the horizontal as well as the vertical. Same hold also for the surface-scattered plane wave. Now, the horizontal components of these two waves cancel each other out, while the vertical component do add up. The remaining scattered wavefield originating from the cavity, however, has no contribution in the horizontal component due to the resulting homogeneous boundary condition at the surface as the refection from the surface is explicitly separated from the scattering wavefield. Thus, since the incoming and scattered wavefield from the surface cancel each other out as they have exactly the opposite contribution in the horizontal direction, the total field has no contribution in the horizontal component as well. The vertical component however has a contribution from the scattering of the cavity. The reflected wave pulse propagates away from the surface, with the same speed and amplitude as the incident wave, and with the same polarity. Note also that at a free (soft) boundary, the restoring force is zero and the reflected wave has the same polarity (no phase change) as the incident wave (Hirose and Lonngren, 1985).

In Figure 8 we show the synthetic spectrogram as well as the seismograms of the scattered wavefield. In the spectrogram one can see that the amplitude is higher near the cavity, since the scattered wave propagates especially like a spherical (here cylindrical) wave, and shows therefore a distance-dependence of the amplitude. The amplitude is the strongest for frequencies higher than 15 Hz, which again reflects the efficiency of scattering. The seismograms show the primary reflected wave as well as some subsequent scattered waves due to internal reflections inside the cavity, which couple out of the cavity a somewhat bit later. The vertical component of the total wavefield is shown in Figure 9. Here, the incident wavefield and the scattered wavefield from the surface add up (and keep the same phase) as mentioned above.

Example for active seismic source

In our second example we tested the case of an incoming spherical wave originating from the surface with an offset of 1500 m distance to the cavity center. For numerical stability, the mesh is not only refined inside the cavity but also towards the origin of the source (see Figure 6). Synthetic traces are not shown in a neighborhood with a radius of 100 m of the source location.

In this case the scattered wavefield includes the scattering from the surface as well as the scattering from the cavity. As the source is located at the surface and propagates radially, the incident wavefield (measured as a spherical wave in the full space) along the surface has a contribution in the horizontal component and no contribution in the vertical component, see Figure 10. Hence, the vertical component has only a contribution of the scattered wavefield from the cavity which also remains in the total wavefield, Figure 11. Again we can see the multiple reflection from inside the cavity. The spectrograms show a more complex structure which is more spread out in the frequency range as well as in distance above the cavity.

For the elastic parameters chosen in this study the condition $kR = 1$ holds for $f \sim 16$Hz. Hence, the system is in the Rayleigh scattering regime for $f \ll 16$ Hz, while the so-called Mie and geometrical scattering are expected for values $f \geq 16$Hz (Skolnik, 1962). For both, incident plane wave observed in the transmission domain and incident spherical wave observed in the back-scattered domain, the incident wavefields have a continuous frequency band, while in the observed scattered fields, the frequency content is low for $f < 16$Hz. Thus the amount of Rayleigh scattering is low compared to the scattering at higher frequencies.

CONCLUSIONS

We have presented a numerical study of the acoustic wave propagation in a 2D-half space containing an inclusion with different acoustic material parameters. The study has used a computational code that can compute the wave propagation in a reliable way, so far in the acoustic limit. We have used high-order FEM with mesh size and polynomial approximation degree chosen in dependence of the problem frequency.

Beside the freedom in choosing the spatial geometry of the model we set up a scheme including the relevant types of seismic sources (point sources and plane wave). Our formulation allows to consider the incident and the scattered wavefields separately. The strength of the approach is that we can compute the wave propagation over a broad range of frequencies. The physical parameters can be varied easily. Our method has also the ability to easily take into account complex geometries/models that include e.g. rubble zones.

From the actually computed scalar, time-harmonic pressure field the full 2-component displacement field is derived. The efficiency of the implementation allows to compute the full wavefield on a large and dense frequency range. The FEM implementation can be used to study the actual dependence of the spectral characteristics from the existence and the properties of an acoustic cavity. Seismograms can be constructed by harmonic composition of the displacement field spectra at each particular point of interest. Here, we focused on acoustic waves (P-wave propagation), respectively, in a 2D half-space. The next steps are to extend the code to a 3D geometry and also to incorporate the full elastic behavior including shear wave propagation. In that way, seismological campaigns can be tested and designed with the objective to find characteristic signals from a cavity in the target region.

ACKNOWLEDGMENT

We acknowledge financial support by the Vienna Science and Technology Fund (WWTF) project MA14-006. This study was initially also supported by the CTBTO and distinguished with the Young Scientist Research Award (YSRA) within their education and outreach initiative. The computational results presented have been achieved in part using the Vienna Scientific Cluster (VSC).

REFERENCES

Adushkin, V. and Spivak, A., 2004, Changes in Properties of Rock Massifs Due to Underground Nuclear Explosions: Combustion, Explosion, and Shock Waves, 40, no. 6, 624–634.

Ainsworth, M., 2004, Discrete Dispersion Relation for hp-Version Finite Element Approximation at High Wave Number: SIAM Journal on Numerical Analysis, 42, no. 2, 553–575.

Antonietti, P. F., Mazzieri, I., Quarteroni, A., and Rapetti, F., 2014, High order space-time discretization for elastic wave propagation problems. In Spectral and High Order Methods for Partial Differential Equations-ICOSAHOM 2012 (pp. 87-97). Springer International Publishing.

Babuška, I. M., and Sauter, S. A., 1997, Is the pollution effect of the FEM avoidable for the Helmholtz equation considering high wave numbers?: SIAM Journal on Numerical Analysis, 34, no. 6, 2392–2423.

Bayliss, A., Goldstein, C. I. and Turkel, E., 1985, On accuracy conditions for the numerical computation of waves: Journal of Computational Physics, 59, 396–404.

Berenger, J., 1994, A perfectly matched layer for the absorption of electromagnetic waves: Journal of Computational Physics, 114, 185–200.

Bin-Mohsin, B. A., 2013, The method of fundamental solutions for Helmholtz-type problems, PhD thesis, University of Leeds.

Bourbié, T., and Coussy, O., 1987, Acoustics of porous media: Institut français du pétrole publications Editions Technip.

Bramble, J. H., and Pasciak, J. E., 2013, Analysis of a cartesian PML approximation to acoustic scattering problems in $\mathbb{R}^2$ and $\mathbb{R}^3$: Journal of Computataional and Applied Mathematics, 247, 209–230.

Cohen, G., 2002, Higher-Order Numerical Methods for Transient Wave Equations: Scientific Computation: Springer-Verlag Berlin Heidelberg.

Colton, D., Kress, R., 1983, Integral Equation Methods in Scattering Theory: Society for Industrial and Applied Mathematics, Classics in Applied Mathematics.

De Basabe, J. D. and Sen, M. K., 2007, Grid dispersion and stability criteria of some common finite-element methods for acoustic and elastic wave equations: Geophysics, 72, no. 6, T81–T95.

Dubiner, M., 1991, Spectral methods on triangles and other domains: Journal of Scientific Computing, 6, no. 4, 345–390.

Esterhazy, S., and Melenk, J. M., 2012, On stability of discretizations of the Helmholtz equation (extended version), Volume 83 of Lecture Notes in Computational Science and Engineering, Springer, Berlin Heidelberg, Berlin, Heidelberg.

Esterhazy, S., and Melenk, J. M., mar 2014, An analysis of discretizations of the Helmholtz equation in and in negative norms: Computers & Mathematics with Applications, 67, no. 4, 830–853.

Faccioli, E., Maggio, F., Paolucci, R., and Quarteroni, A., 1997, 2D and 3D elastic wave propagation by a pseudo-spectral domain decomposition method: Journal of seismology, 1, no. 3, 237–251.

Gritto, R., 2003, Subsurface void detection using seismic tomographic imaging: Lawrence Berkeley National Laboratory.

Hirose, A., and Lonngren, K. E., 1985, Introduction to wave phenomena: Wiley-Interscience.

Ihlenburg, F., and Babuška, I., 1995, Finite element solution of the Helmholtz equation with high wave number Part I: The h-version of the FEM: Computers & Mathematics with Applications, 30, no. 9, 9–37.

Imhof, M. G., 2004, Computing the elastic scattering from inclusions using the multiple multipoles method in three dimensions: Geophysical Journal International, 156, no. 2, 287–296.

Komatitsch, D. and Vilotte, J.-P., 1998,The spectral element method: An efficient tool to simulate the seismic response of 2D and 3D geological structures. Bulletin of the Seismological Society of America, 88, 368—392.

Komatitsch, D. and Tromp, J., 2002a, Spectral-element simulations of global seismic wave propagation - I. Validation, Geophysical Journal International, 149, 390—412.

Korneev, V. A., and Johnson, L. R., 1993, Scattering of Elastic Waves by a Spherical Inclusion. I. Theory and Numerical Results: Geophysical Journal International, 115, no. 1, 230–250.

Korneev, V. A., and Johnson, L. R., 1993, Scattering of elastic waves by a spherical inclusion-11. Limitations of asymptotic solutions: Geophysical Journal International, 115, no. 1, 251-263.

Korneev, V. A., 2009, Resonant seismic emission of subsurface objects: Geophysics, 74, no. 2, T47–T53.

McLean, W.C.H., 2000, Strongly Elliptic Systems and Boundary Integral Equations: Cambridge University Press.

Mei, C. C., Si, B. I., and Cai, D., 1984, Scattering of simple harmonic waves by a circular cavity in a fluid-infiltrated poro-elastic medium: Wave Motion, 6, no. 3, 265–278.

Melenk, J. M., and Sauter, S., 2010, Convergence analysis for finite element discretizations of the Helmholtz equation with Dirichlet-to-Neumann boundary conditions: Mathematics of Computation, 79, no. 272, 1871–1871.

Melenk, J. M., and Sauter, S., 2011, Wavenumber Explicit Convergence Analysis for Galerkin Discretizations of the Helmholtz Equation: SIAM Journal on Numerical Analysis, 49, no. 3, 1210–1243.

Pointer, T., Liu, E. and Hudson, J. A., 1998, Numerical modeling of seismic waves scattered by hydrofractures: application of the indirect boundary element method: Geophysical Journal International, 135, no. 1, 289–303.

Rechtien, R. D., Stewart, D. M., and Cavanaugh, T. D., Seismic detection of subterranean cavities, Technical report, Missouri University, Rolla, Department of Geology, 1976.

Richards, P. G., and Zavales, J., 1990, Seismic discrimination of nuclear explosions: Annual Review of Earth and Planetary Sciences, 18, 257.

Schöberl, J., 1997, Netgen an advancing front 2D/3D-mesh generator based on abstract rules: Computing and visualization in science, 1, no. 1, 41–52.

Schöberl, J., C++ 11 implementation of finite elements in ngsolve:, Technical report, Institute for Analysis and Scientific Computing, TU Wien, 2014.

Seriani, G. and Priolo, E., 1994, Spectral element method for acoustic wave simulation in heterogeneous media: Finite Elements in Analysis and Design, 16, no. 3–4, 337–348.

Sherwin, S. J., and Karniadakis, G. E., 1995, A triangular spectral element method; applications to the incompressible Navier-Stokes equations: Computer methods in applied mechanics and engineering, 123, no. 1-4, 189–229.

Sloan, S. D., Peterie, S. L., Miller, R. D., Ivanov, J., Schwenk, J. T., and McKenna, J. R., 2015, Detecting clandestine tunnels using near-surface seismic techniques: Geophysics, 80, no. 5, EN127–EN135.

Skolnik, M. I., 1962, Introduction to Radar Systems: McGraw-Hili book company.

Tran, K. T., McVay, M., Faraone, M., and Horhota, D., 2013, Sinkhole detection using 2D full seismic waveform tomography: Geophysics, 78, no. 5, R175–R183.

Yokoi T., Sánchez-Sesma, F. J., 1998, A hybrid calculation technique of the Indirect Boundary Element Method and the analytical solutions for three-dimensional problems of topography: Geophysical Journal International, 133, no. 1, 121–139.

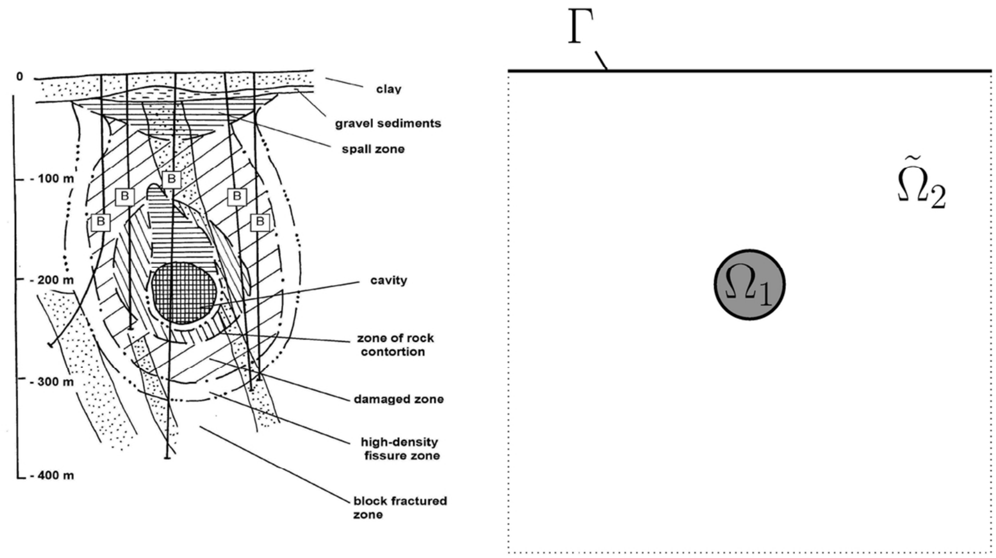

1 Left: Subsurface structure after an underground nuclear explosion (Adushkin and Spivak, 2004). Right: Simple design of a homogeneous medium surrounding a spherical cavity.

104x63mm (300 x 300 DPI)

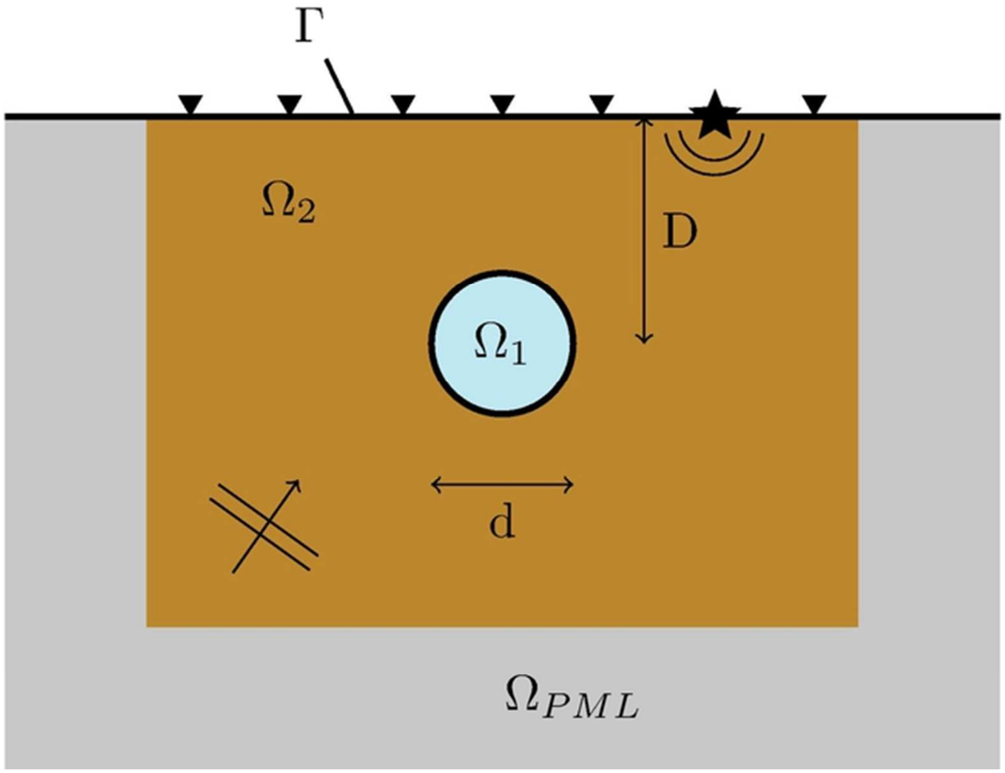

2 Geometry with PML region for numerical computation. The star indicates an active seismic source, while triangles represent seismometers.

54x42mm (300 x 300 DPI)

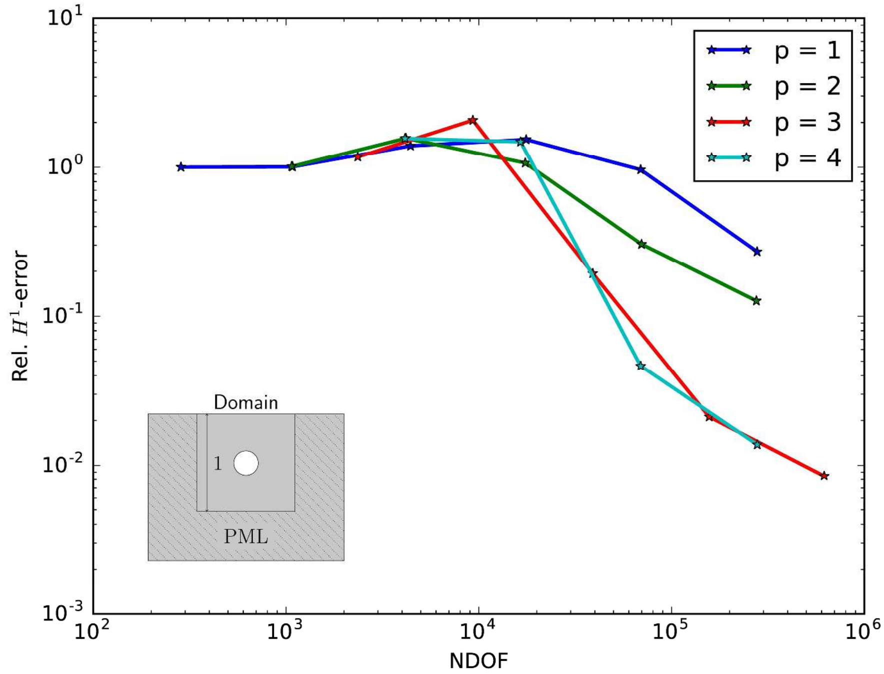

3 Convergence analysis on a geometry given by a unit square containing a circular vacuum-cavity with radius a = 0.25. With the Dirichlet boundary condition imposed on the top the other sides are surrounded by a PML of width L = 3. The wavenumber is k = 30 and physical parameters are set to one, i.e. (v = ρ = 1). Hence, there are 7 and 28 waves in the domain of interest and the whole domain including the PML, respectively; the FEM-solutions for p = 1,2,3,4 are tested again a reference solution of polynomial degree p = 6 on a very fine mesh (again 6 refinements).

307x230mm (300 x 300 DPI)

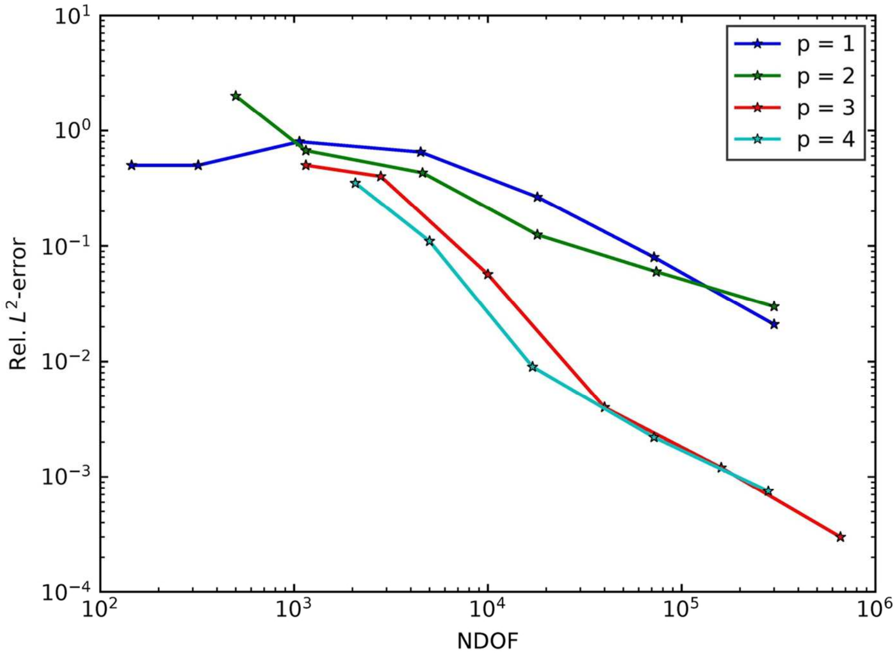

4 Convergence analysis on a geometry given by a unit square containing a circular vacuum-cavity with radius a = 0.25, surrounded by a PML-layer of width L = 1. The wavenumber is k = 10π and physical parameters are set to two, i.e. (v = ρ = 2). Hence, there are 5 and 10 waves in the domain of interest and the whole domain including the PML, respectively; the FEM-solutions for p = 1,2,3,4 are tested again the exact solution on a very fine mesh (h=0.01).

122x92mm (300 x 300 DPI)

5 Decrease of the scattered wavefield evaluated at the depth of 600 m on the right side of the perfectly matched layer (see red dots in the domain thumbnail).

1120x868mm (600 x 600 DPI)

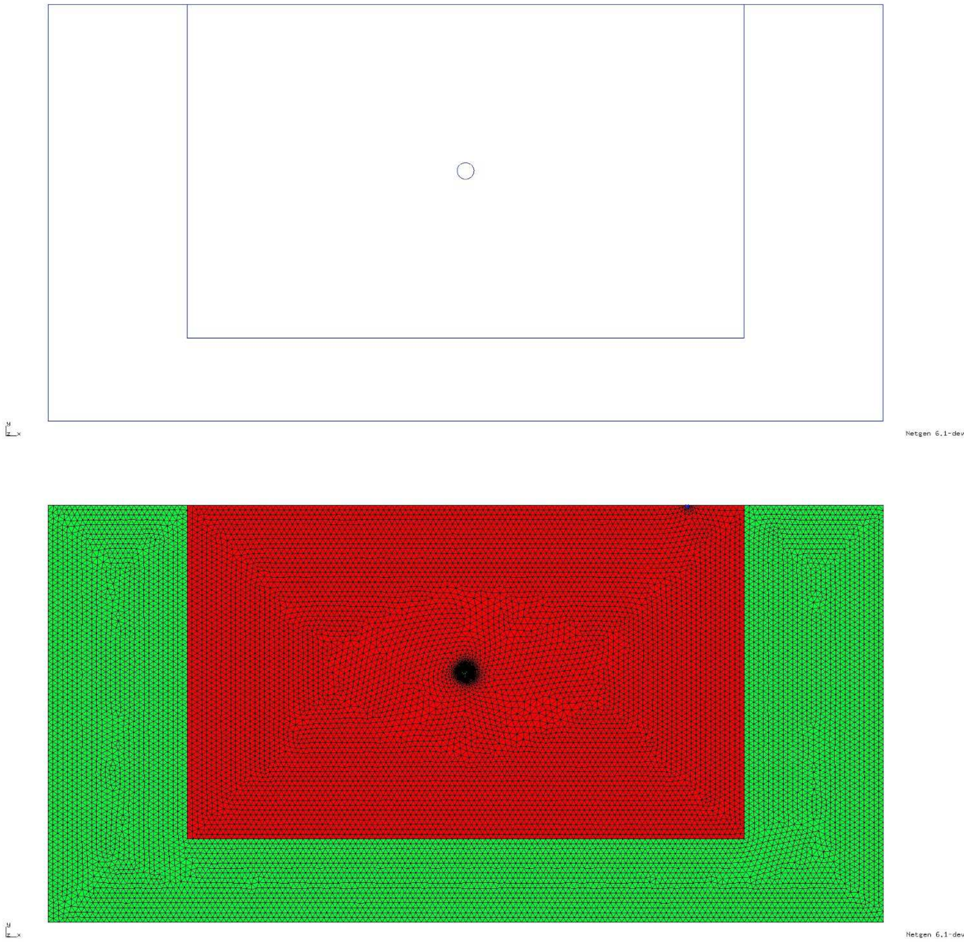

6 Top: Geometry of the cavity design build in Netgen. Bottom: Mesh with refinement in the cavity and the source point.

302x305mm (300 x 300 DPI)

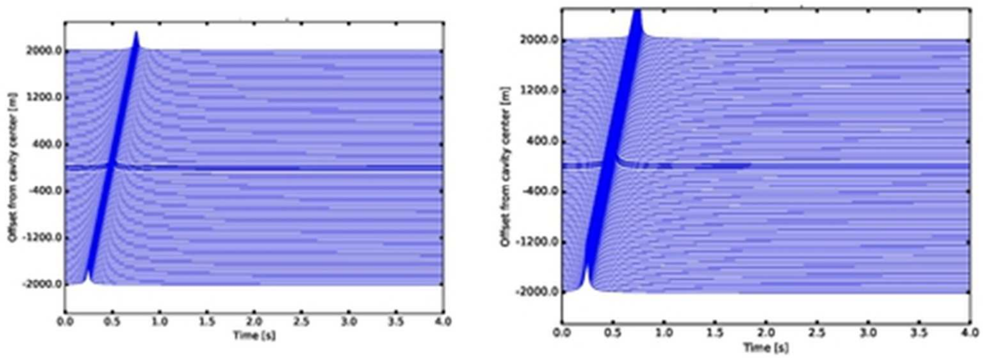

7 Synthetic seismograms of the horizontal component (left) and vertical component (right) of the incoming plane wavefield.

42x16mm (300 x 300 DPI)

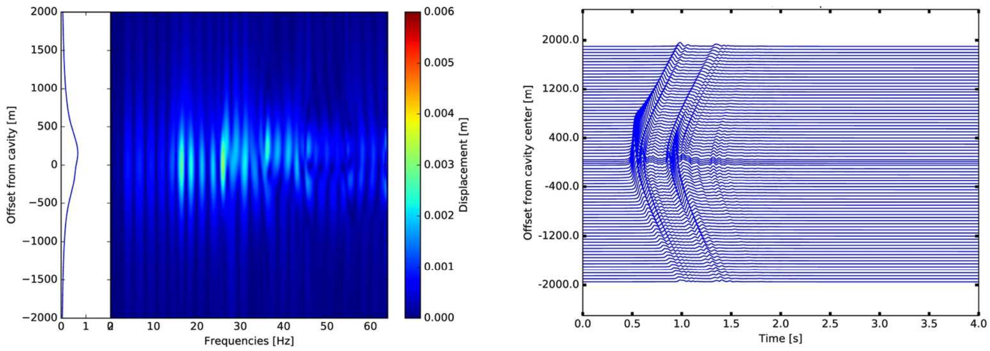

8 Synthetic spectrograms (left) and seismograms (right) of the vertical component of the scattered wavefield from the cavity, measured at the surface. The curve left of the spectrogram displays the spatial distribution of the scattered field amplitude averaged over all frequencies.

142x51mm (300 x 300 DPI)

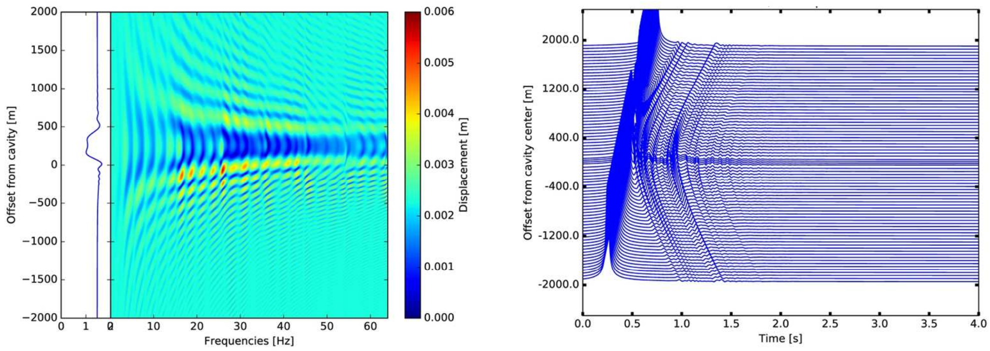

9 Synthetic spectrograms (left) and seismograms (right) of the vertical compo- nent the total wavefield, measured at the surface. The curve left of the spectrogram displays the spatial distribution of the total field amplitude averaged over all frequencies.

142x51mm (300 x 300 DPI)

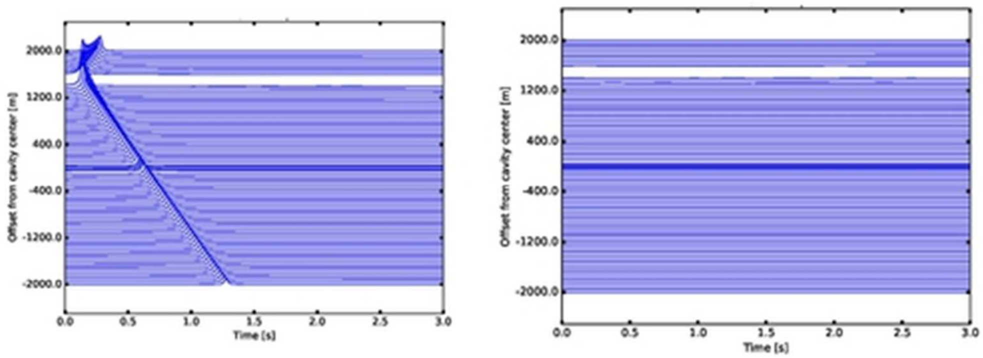

10 Synthetic seismograms of the horizontal component (left) and vertical component (right) of the incoming spherical wavefield.

42x16mm (300 x 300 DPI)

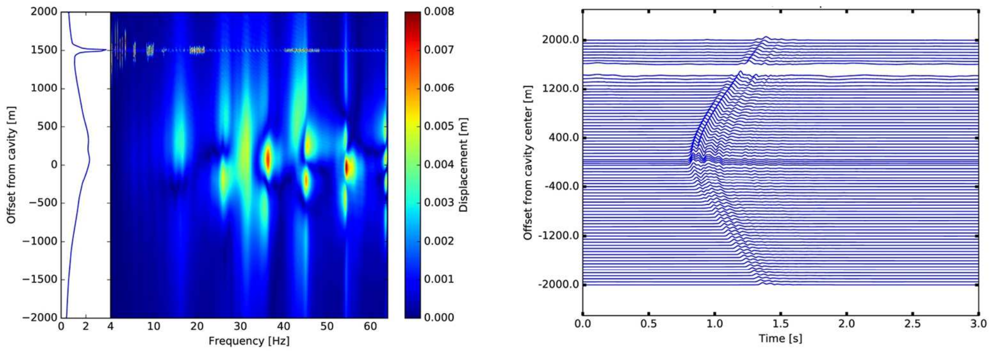

11 Synthetic spectrograms (left) and seismograms (right) of the vertical component of the scattered wavefield from the cavity, measured at the surface, which is identical to the total wavefield. The curve left of the spectrogram displays the spatial distribution of the scattered field amplitude averaged over all frequencies.

142x51mm (300 x 300 DPI)